Trans. JWRI, Vol. 25(1996), No.2

Metallo-Thermo-Mechanics

Application to Phase Transformation incorporated Processes

by Tatsuo Inoue

Department of Energy Conversion Science Graduate School of Energy Science, Kyoto University, Yoshida-Honmachi, Sakyo-ku, Kyoto, Japan

Abstract

Fundamental equations governing the evolution of metallurgical structures, temperature, and stress/strain relevant to describing both in-solid and liquid-solid phase transformation are formulated by taking into account the effect of metallo-thermo-mechanical coupling. The inelastic constitutive equations are established and applied to numerical simulation of some engineering processes such as quenching, welding and casting by means of the finite element technique.

1. Introduction

The effect of coupling between metallic structures, including the molten state, temperature, and stress and/or strain occurring in processes accompanied by phase transformation, sometimes plays an important role in such industrial processes as quenching, welding and continuous casting. **Figure 1** represents the schematic features of the effect of metallo-thermo-mechanical coupling with the induced phenomena[1-5]. When the temperature distribution in a material varies, thermal stress ① is caused in the body, and the induced phase transformation ② affects the structural distribution, which is known as melting or solidification in solid-liquid transition and pearlite or martensite transformation in the solid phase. Local dilatation due to structural changes in the body bring out the transformation stress ③, and interrupts the stress or strain field in the body.

In contrast to these phenomena, which are well known in ordinal analysis, arrows in the opposite direction indicate coupling in the following manner. Part of the mechanical work done by the existing stress in the material is converted into heat ④, which may be predominant in the case of inelastic deformation, thus disturbing the temperature distribution. The acceleration of phase transformation by stress or strain, which is called stress- or strain-induced transformation ⑤, has been discussed by metallurgists as one of leading parameters of transformation kinetics. The arrow numbered by ⑥ corresponds to the latent heat due to phase transformation, which are essential in deter-mining the temperature. The purpose of this paper is to present a method that simulates such processes involving phase transformation when considering the effect of the coupling just mentioned. Formulation of the fundamental equations for stress-strain relationships, heat conduction and transfor-mation kinetics based on continuum thermo-dynamics will be done in the first part, and some examples of the numerical simulation of temperature,

Transactions of JWRI is published by Joining and Welding Research Institute of Osaka University, Ibaraki, Osaka567, Japan.

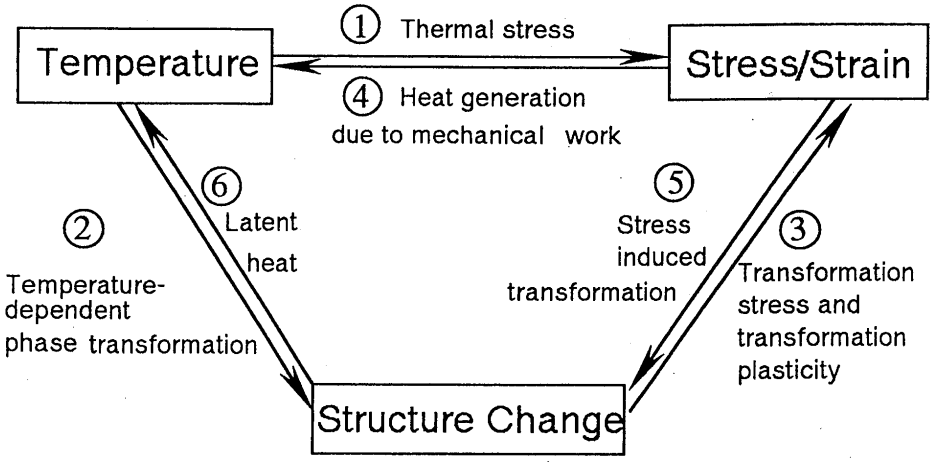

Fig. 1 Triangle indicating metallo-thermo-coupling.

stress/strain and metallic structures in the processes of quenching, welding and casting will be presented.

2. Fundamental Framework of the Governing Equations

Consider a material undergoing structural change due to phase transformation as a mixture of N kinds of constituents[6]. Denoting the volume fraction of the I th constituent as ξ_I(See **Fig.2**), the physical and mechanical properties x of the material are assumed to be a linear combination of the properties x_I of the constituent as

$$x = \sum_{I=1}^{N} x_I \xi_I , \tag{1}$$

with

$$\sum_{I=1}^{N} \xi_I = 1, \tag{2}$$

Where $\sum_{I=1}^{N}$ is the summation for suffix I from 1 to N. All material parameters appearing below are defined in the manner of Eq.(1)

The Gibbs free-energy density function $G$is defined as

$$G = U - T\eta - \frac{1}{\rho}\sigma_{ij}\varepsilon_{ij}^{e} , \tag{3}$$

where U, T, η and ρ are the internal energy density, temperature, entropy density and mass

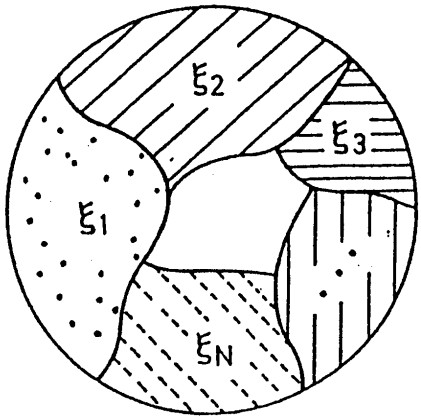

Fig. 2 Concept of mixture.

density, respectively. Elastic strain rate $\dot{\varepsilon}_{ij}^{e}$ in Eq. (3) is defined as the subtraction of inelastic strain rate $\dot{\varepsilon}_{ij}^{i}$ ' from total strain rate $\dot{\varepsilon}_{ij}$ ', that is,

$$\dot{\varepsilon}_{ij}^{e} = \dot{\varepsilon}_{ij} , - \dot{\varepsilon}_{ij}^{i} \tag{4}$$

The thermodynamic state of a material is assumed to be determined by stress σ_{ij}, temperature T, temperature gradient g_i(= grad T) and a set of internal variables of inelastic strain ε_{ij}^{i}, back stress α_{ij} 'and hardening parameter k related to inelastic deformation, together with the volume fraction of the constituents ξ_I. Then, the general form of the constitutive equation can be expressed as

$$G = G\left(\sigma_{ij}, T, g_i, \varepsilon_{ij}^{i}, \alpha_{ij}, \kappa, \xi_I\right) , \tag{5}$$

$$\eta = \eta\left(\sigma_{ij}, T, g_i, \varepsilon_{ij}^{i}, \alpha_{ij}, \kappa, \xi_I\right) , \tag{6}$$

$$q_i = q_i\left(\sigma_{ij}, T, g_i, \varepsilon^i_{ij}, \alpha_{ij}, \kappa, \xi_I\right), \tag{7}$$

$$\varepsilon^e_{ij} = \varepsilon^e_{ij}\left(\sigma_{ij}, T, g_i, \varepsilon^i_{ij}, \alpha_{ij}, \kappa, \xi_I\right), \tag{8}$$

Here, q_i is the heat flux. The evolution equations for the internal variables are defined in the same form as Eqs. (5)-(8), i.e.

$$\dot{\varepsilon}^i_{ij} = \dot{\varepsilon}^i_{ij}\left(\sigma_{ij}, T, g_i, \varepsilon^i_{ij}, \alpha_{ij}, \kappa, \xi_I\right), \tag{9}$$

$$\dot{\alpha}_{ij} = \dot{\alpha}_{ij}\left(\sigma_{ij}, T, g_i, \varepsilon^i_{ij}, \alpha_{ij}, \kappa, \xi_I\right), \tag{10}$$

$$\dot{\kappa} = \dot{\kappa}\left(\sigma_{ij}, T, g_i, \varepsilon^i_{ij}, \alpha_{ij}, \kappa, \xi_I\right), \tag{11}$$

$$\dot{\xi}_I = \dot{\xi}_I\left(\sigma_{ij}, T, g_i, \varepsilon^i_{ij}, \alpha_{ij}, \kappa, \xi_I\right), \tag{12}$$

When the strong form of the Clausius-Duhem inequality

$$-\rho\left(\dot{G} + \eta\dot{T}\right) - \dot{\sigma}_{ij}\varepsilon^e_{ij} + \sigma_{ij}\dot{\varepsilon}^i_{ij} \geq 0, \tag{13}$$

with

$$g_i q_i \leq 0, \tag{14}$$

is applied, the constitutive relationships in Eqs. (5-8) are reduced to

$$G = G\left(\sigma_{ij}, T, \varepsilon^i_{ij}, \alpha_{ij}, \kappa, \xi_l\right), \tag{15}$$

$$\varepsilon^e_{ij} = \rho\frac{\partial}{\partial\sigma_{ij}} G\left(\sigma_{ij}, T, \varepsilon^i_{ij}, \alpha_{ij}, \kappa, \xi_l\right), \tag{16}$$

$$\eta = -\rho\frac{\partial}{\partial T} G\left(\sigma_{ij}, T, \varepsilon^i_{ij}, \alpha_{ij}, \kappa, \xi_l\right), \tag{17}$$

$$q_i = -k\left(\sigma_{ij}, T, \varepsilon^i_{ij}, \alpha_{ij}, \kappa, \xi_l\right)g_i, \tag{18}$$

Here, Fourier's law has been used in Eq.(18) with thermal conductivity k.

3. Stress-Strain Constitutive Equation

To obtain an explicit expression for the elastic strain in Eq. (16), the Gibbs free-energy G is assumed to be determined by that of constituent G_I in the form of Eq. (1) as

$$G\left(\sigma_{ij}, T, \varepsilon^i_{ij}, \alpha_{ij}, \kappa, \xi_I\right) = \sum_{I=1}^{N} \xi_I G_I\left(\sigma_{ij}, T, \varepsilon^i_{ij}, \alpha_{ij}, \kappa,\right) \tag{19}$$

When G_I is divided into the elastic and inelastic parts as

$$G_I\left(\sigma_{ij}, T, \varepsilon^i_{ij}, \alpha_{ij}, \kappa, \xi_I\right) = G^e_I\left(\sigma_{ij}, T\right) + G^i_I\left(T, \varepsilon^i_{ij}, \alpha_{ij}, \kappa\right) \tag{20}$$

we can derive the elastic strain from Eq. (16) by expanding elastic part G^e_I around the natural state, $\sigma_{ij} = 0$ and $T = T_0$, in terms of the representation theorem for an isotropic function;

$$\varepsilon^e_{ij} = \left(\sum_{I=1}^{N}\frac{1+\nu_I}{E_I}\xi_I\right)\sigma_{ij} - \left(\sum_{I=1}^{N}\frac{\nu_I}{E_I}\xi_I\right)\delta_{ij}\sigma_{kk} + \delta_{ij}\int_{T_0}^{T}\sum_{I=1}^{N}\alpha_I\xi_I dT + \delta_{ij}\sum_{I=1}^{N}\beta_I\left(\xi_I - \xi_{I0}\right) \tag{21}$$

Here, E_I, ν_I, α_I and β_I correspond to Young's modulus, Poisson's ratio, thermal expansion coeffcient and dilatation of the I th constituent, respectively.

3.1 Plastic Strain Rate

Assume that the evolution of back stress α_{ij} of the yield surface and hardening parameter κ can be determined by

$$\dot{\alpha}_{ij} = C\left(T, \kappa, \xi_I\right)\dot{\varepsilon}^i_{ij} \tag{22}$$

$$\dot{\kappa} = \bar{\dot{\varepsilon}}^i = \left(\frac{2}{3}\dot{\varepsilon}^i_{ij}\dot{\varepsilon}^i_{ij}\right)^{1/2} \tag{23}$$

where $\bar{\dot{\varepsilon}}^i$ represents the equivalent inelastic strain rate. To take into account the effect of changing structural fraction ξ_I, we take the form of the yield function as

$$F = F\left(\sigma_{ij}, T, \varepsilon^i_{ij}, \xi_I\right) = \left[\frac{2}{3}\left(s_{ij} - \alpha_{ij}\right)^2\right]^{1/2} - K\left(T, \kappa, \xi_I\right) \tag{24}$$

where $s_{ij}\left(\sigma_{ij} - \frac{1}{3}\delta_{ij}\sigma_{kk}\right)$ represents the deviatoric stress component. Employing the normality rule and the consistency relationship, the final form of the time-independent inelastic strain rate, or plastic strain rate, reads.

$$\dot{\varepsilon}^i_{ij} = \Lambda\frac{\partial F}{\partial\sigma_{ij}}$$

$$= \hat{G}\left(\frac{\partial F}{\partial \sigma_{kl}}\dot{\sigma}_{kl} + \frac{\partial F}{\partial T}\dot{T} + \sum_{I=1}^{N}\frac{\partial F}{\partial \xi_I}\dot{\xi}_I\right)\frac{\partial F}{\partial \sigma_{ij}} \tag{25}$$

with

$$\frac{1}{\hat{G}} = -\left\{\frac{\partial F}{\partial \sigma_{mn}}\frac{\partial F}{\partial \varepsilon^i_{mn}} + \frac{\partial F}{\partial \sigma_{mn}}\frac{\partial F}{\partial \alpha_{mn}} + \left(\frac{2}{3}\frac{\partial F}{\partial \sigma_{mn}}\frac{\partial F}{\partial \sigma_{mn}}\right)^{1/2}\frac{\partial F}{\partial \kappa}\right\} \tag{26}$$

Equation (25) means that plastic strain is induced not only by stress, but also by the temperature and phase change.

3.2 Viscoplastic Strain Rate

The elastic-plastic constitutive relationship is suitable for describing the material behavior at relatively low temperature. However, time-dependency or viscosity might predominate at higher temperature level, particularly when the material behaves like a viscous liquid beyond its melting point. In order to analyze such processes as welding and casting, in which melting and/or solidification of the metal are essential phenomena, adequate formulation of the viscoplastic constitutive model is needed. Malvern[7] and Perzyna[8] proposed a viscoplastic constitutive equation for time-dependent inelastic strain rate $\dot{\varepsilon}^i_{ij}$ in the form.

$$\dot{\varepsilon}^i_{ij} = \frac{1}{3\mu}\langle\psi(F)\rangle\frac{\partial F}{\partial \sigma_{ij}} \tag{27}$$

with the static yield function

$$F = \frac{f\left(\sigma_{ij}, T, \varepsilon^i_{ij}\right)}{K} - 1 \tag{28}$$

where μ and K denote the stress, and coefficient of viscosity and the static flow, and

$$\langle\psi(F)\rangle = \begin{cases} 0, & \text{if } \psi(F) \le 0 \\ \psi(F), & \text{if } \psi(F) > 0 \end{cases} \tag{29}$$

Equation (27) indicates that the inelastic strain rate is induced in an outer direction normal to static yield surface F, and that the magnitude of the strain rate depends on the ratio of excess stress (f-K) to flow stress K. If we adopt the flow rule (Eq. (27)) to the liquid state, the flow stress tends to vanish ($K \to 0$) and the yield surface F expands infinitely ($F \to \infty$), which implies that the strain rate is infinite at low stress. To compensate for such an inconsistency occurring in a liquid, a modification to Eq. (28) is made such that

$$F = f\left(\sigma_{ij}, T, \varepsilon^i_{ij}\right) - K\left(T, \kappa, \xi_I\right) \tag{30}$$

When we take the simple forms of functions ψ and F

$$\psi(F) = F \tag{31}$$

$$F = \left[\frac{3}{2}\left(s_{ij} - \alpha_{ij}\right)\left(s_{ij} - \alpha_{ij}\right)\right]^{1/2} - K\left(T, \kappa, \xi_I\right) \tag{32}$$

Eq.(27) can be reduced to

$$\dot{\varepsilon}^i_{ij} = \frac{1}{2\mu}\left\langle 1 - \frac{K\left(T, \kappa, \xi_I\right)}{\left[3\left(s_{kl} - \alpha_{kl}\right)\left(s_{kl} - \alpha_{kl}\right)\right]^{1/2}}\right\rangle\left(s_{ij} - \alpha_{ij}\right) \tag{33}$$

This constitutive relationship may be relevant to a liquid-solid transition region with high viscosity, as well as to a normal time-independent plastic body[9]. For instance, when flow stress K equals zero in Eq. (33), the total strain rate $\dot{\varepsilon}_{ij}$ ($= \dot{\varepsilon}^e_{ij} + \dot{\varepsilon}^i_{ij}$;) is given by

$$\dot{\varepsilon}_{ij} = \frac{1+\nu}{E}\dot{\sigma}_{ij} - \frac{\nu}{E}\dot{\sigma}_{kk}\delta_{ij} + \frac{1}{2\mu}s_{ij} \tag{34}$$

when the effect of temperature and phase change is neglected for simplicity. This equation is equivalent to the Maxwell constitutive model for a viscoelastic body.

When the elastic component of shear deformation is small enough compared with the viscoplastic component, as is usual for a viscous fluid, the Newtonia fluid model

$$\sigma_{ij} = 2\mu\dot{\varepsilon}_{ij} - \frac{2}{3}\mu\dot{\varepsilon}_{kk}\delta_{ij} - p\delta_{ij}, \quad p = -\frac{1}{3}\sigma_{kk} \tag{35}$$

is obtainable from Eq. (34) by neglecting the

elastic shear strain rate. Furthermore, when the elastic volume dilatation ε^e_{kk} is removed from Eq. (35), we have

$$\sigma_{ij} = 2\mu\dot{\varepsilon}_{ij} - p\delta_{ij} \tag{36}$$

which represents the model for an incompressible Newtonian fluid. In the limiting case for an inviscid material (μ=0), $\psi(F)$ in Eq. (27) tends to infinity and

$$\frac{1}{3\mu}\psi(F) \equiv \Lambda = const. \tag{37}$$

should hold to give the form

$$\dot{\varepsilon}^i_{ij} = \Lambda\frac{\partial F}{\partial \sigma_{ij}} \tag{38}$$

Parameter Λ can be easily determined by applying the consistency relationship, and thus we get back again to the previous discussion for time-independent plastic strain. From the considerations just mentioned, the constitutive relationship developed in Eq. (33) seems to be useful for a wide range of metals from inelastic solids to viscous fluids.

4. Heat Conduction Equation

When we adopt Eqs. (15)-(18) to the energy conservation law

$$\rho\dot{U} - \sigma_{ij}\dot{\varepsilon}_{ij} + \frac{\partial q_i}{\partial x_I} = 0 \tag{39}$$

the equation of heat conduction

$$\rho c\dot{T} - k\frac{\partial^2 T}{\partial x_I \partial x_I} + \rho\sum_{I=1}^{N} l_I\dot{\xi}_I + T\frac{\partial \varepsilon^e_{ij}}{\partial T}\dot{\sigma}_{ij} + \left(\rho\frac{\partial H}{\partial \varepsilon^i_{ij}}\dot{\varepsilon}^i_{ij} + \rho\frac{\partial H}{\partial \alpha_{ij}} + \rho\frac{\partial H}{\partial \kappa}\dot{\kappa} - \sigma_{ij}\dot{\varepsilon}^i_{ij}\right) = \rho r \tag{40}$$

holds with enthalpy density H (=G+T η) and latent heat l_I due to the increase of the Ith phase

$$l_I = \frac{\partial H}{\partial \xi_I} \tag{41}$$

The fifth term on the left-hand side of Eq. (40) denotes the heat generation by inelastic dissipation, which is significant when compared with the elastic work represented by the fourth term, and the third term arises from the latent heat through phase changes. Hence, it can be seen that Eq. (40) corresponds to the ordinal equation of heat conduction, provided that these terms are neglected.

5. Kinetics of Phase Transformation

During phase transformation, a given volume of material is assumed to be composed of several kinds of constituent ξ_I as expressed in Eq. (1). We choose four kinds of volume fraction: liquid ξ_L, austenite ξ_A, pearlite ξ_P and mar-tensite ξ_M, and other structures induced by precipitation by recovery effect, say during annealing process. When austenite is cooled in equilibrium, bainite, ferrite and carbite are produced in addition to pearlite, but for brevity all these structures resulting from a diffusion type of transformation are called as pearlite. The nucleation and growth of pearlite in an austenitic structure are phenomenologically governed by the mechanism for a diffusion process, and Johnson and Mehl[10] proposed a formula for volume fraction ξ_P as

$$\xi_P = 1 - \exp(-V_e) \tag{42}$$

where V_e means the extended volume of the pearlitic structure given by

$$V_e = \int_0^t \frac{4}{3}\pi R(t-\tau)^3 n\,d\tau \tag{43}$$

Here, R is the moving rate of the surface of pearlite. Bearing in mind that the value of R is generally a function of stress as well as temperature, Eq. (43) may be reduced to

$$V_e \int_0^t f(T,\sigma_{ij})(t-\tau)^3\,d\tau \tag{44}$$

Function f(T, 0) can be determined by fitting the temperature-time-transformation (TTT) diagram or continuous-cooling transformation (CCT) diagram without stress, and $f(T,\sigma_{ij})$ may be given by the start-time or finish-time data for pearlite transformation with an applied stress, an example of which is shown in **Fig.3**[12].

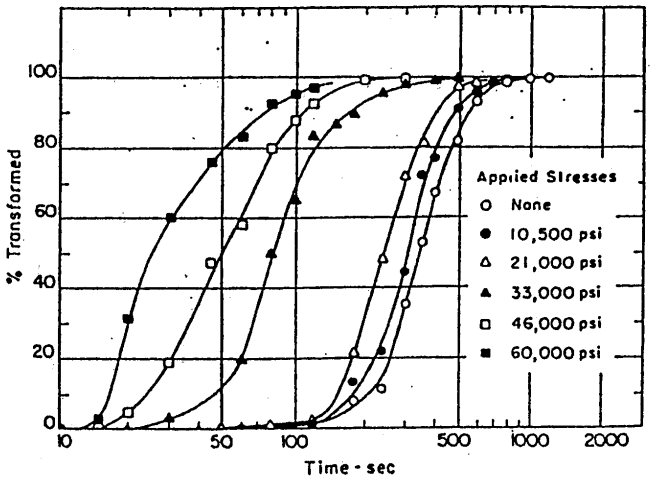

Fig. 3 Pearlite fraction accelerated by applied stress.

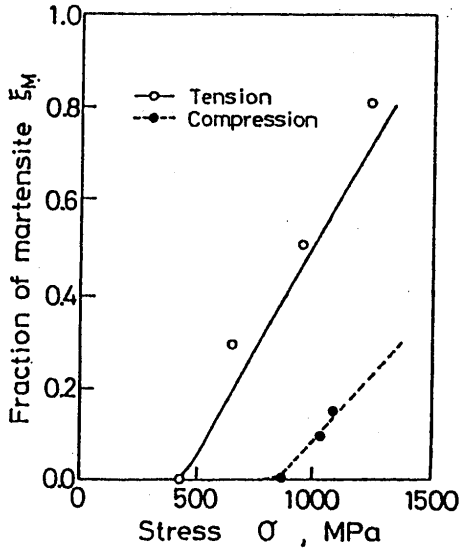

Fig. 4 Martensite depending on stress.

The empirical relationship for the austenite -martensite transformation is also obtainable by modifying the kinetic theory of Magee[11]. Assume that the grow th of a martensite structure is a linear function of the increase of the difference ΔG in free-energy between austenite and martensite as

$$d\xi_M = -\bar{v}(1-\xi_M)\phi d(\Delta G) \qquad (45)$$

Regarding the free-energy G as a function of temperature and stress, we can obtain the form of ξ_M by integrating Eq. (45) as

$$\xi_M = 1-\exp\left[\phi_1(T-M_s)+\phi_2(\sigma_{ij})\right] \qquad (46)$$

The function $\phi_2(\sigma_{ij})$ is identified by the such data as shown in **Fig. 4**[14].

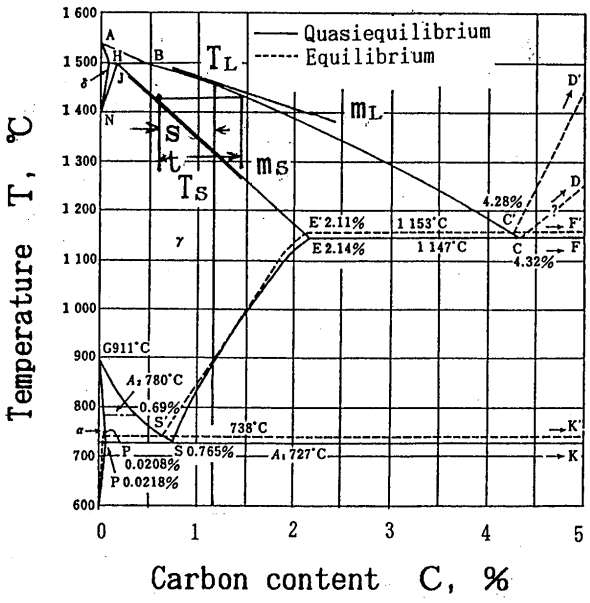

Fig. 5 Example of phase diagram.

For the rate of solidification, we employ the well-known lever rule(See **Fig. 5** as an example),and the volume fraction of austenite is

$$\xi_A = \frac{(T_L - T)/m_L}{(T-T_A)/m_A + (T_L - T)/m_L} \qquad (47)$$

where T_L and T_A denote the liquidus and solidus temperatures, respectively, and m_L and m_A are gradients of the liquidus and solidus temperatures with respect to the carbon content in the phase diagram.

6. Finite Element Simulation of Some Engineering Processes

Simulation of some typical engineering processes involving phase transformation is possible by the finite element method when the fundamental equations developed here are adopted.

6.1 Heat treatment

Series of equations summarized above are to be numerically solved by the finite element

method. The authors developed a finite element CAE system "HEARTS" (HEAt tReaTment Simulation program), which is available for the analysis of heat treatment process in this stage[14-17]. The system HEARTS is designed based on the implementation procedure for the finite element technique developed by K. J. Bathe[18]. This procedure is proposed for developing a program for practical use which can analyze very large systems and add some different types of element and kinds of function without difficulty. The time integration in the heat conduction and other diffusin analyses employ α-method which is reduced to the trapezoid and Euler backward methods, in the special cases. Nonlinear equations in each analysis are made by the Newton's iteration method.

The followings are some examples of simulated results carried out by the HEARTS.

Carburized water quenching of a cylinder

The first example is the carburized water quenching of a long cylinder of a case-hardening steel containing molybdenum[14]. The cylinder of 8mm diameter is treated by modeling into a series of elements in the radial direction and by applying the generalized plain stress condition for the stress/strain analysis. Temperature dependent material data necessary for heat conduction and stress/strain analyses are piled up in the material data file also being the function of metallic structures.

For the simulation of carburized quenching, normally processed in advanced to quenching, a simple diffusion equation,

$$\frac{\partial C}{\partial t} = D\frac{\partial^2 C}{\partial x_i \partial x_j} \qquad (48)$$

is required to be solved in order to determine the distribution of carbon content C. Here, D is diffusion constant generally depending on temperature, carbon content, stress/strain and volume fraction of each structure.

Solid line in **Fig. 6** represents the result of distribution of carbon content after carburization, which gives fairly good agreement with measured data by the X-ray diffraction technique indicated by circles. **Figures 7** and **8** shows volume fraction of metallic structures and residual stresses distributions, respectively.

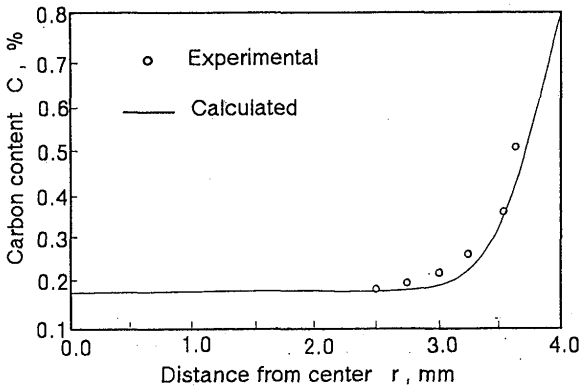

Fig. 6 Distribution of diffused carbon content.

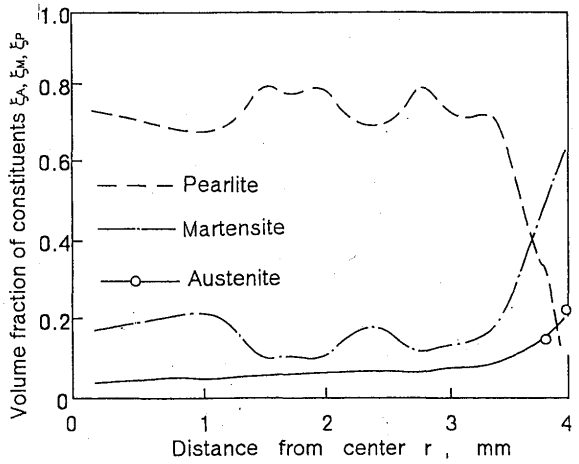

Fig. 7 Structure distribution after quenching.

Carburized oil quenching of a gear

Carburized quenching process of a gear tooth is treated as the second example[14]. The gear is an involute type with pressure angle of 20 degree, 90 number of teeth, 3 in module, 277.11 mm in outer diameter and 40 mm in tooth width. The numbers of nodal points and elements of the model is 1,369 and 932, respectively, and 8-nodal points isoparametric element is used.

The material is a nickel-chromium steel. The carburizing process consists of 210 min. carburizing stage and 63 min. diffusion stage. The boundary conditions for carburization of carbon are assumed such that no carbon diffusion occurs from the external environments via radial direction surfaces on the tip and bottom of the tooth. It is also assumed in the carburizing stage that the carbon content in

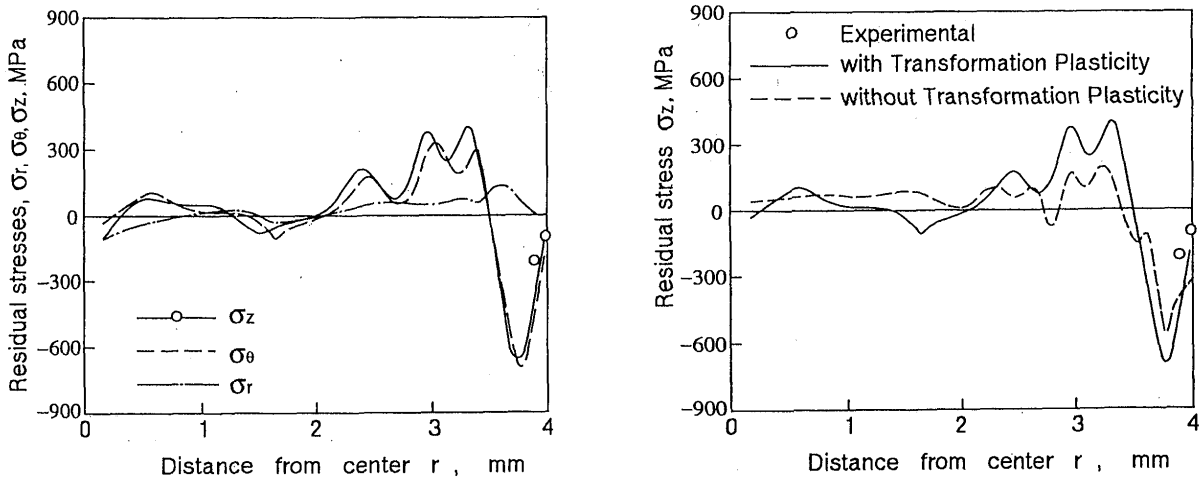

Fig. 8 Residual stress distribution.

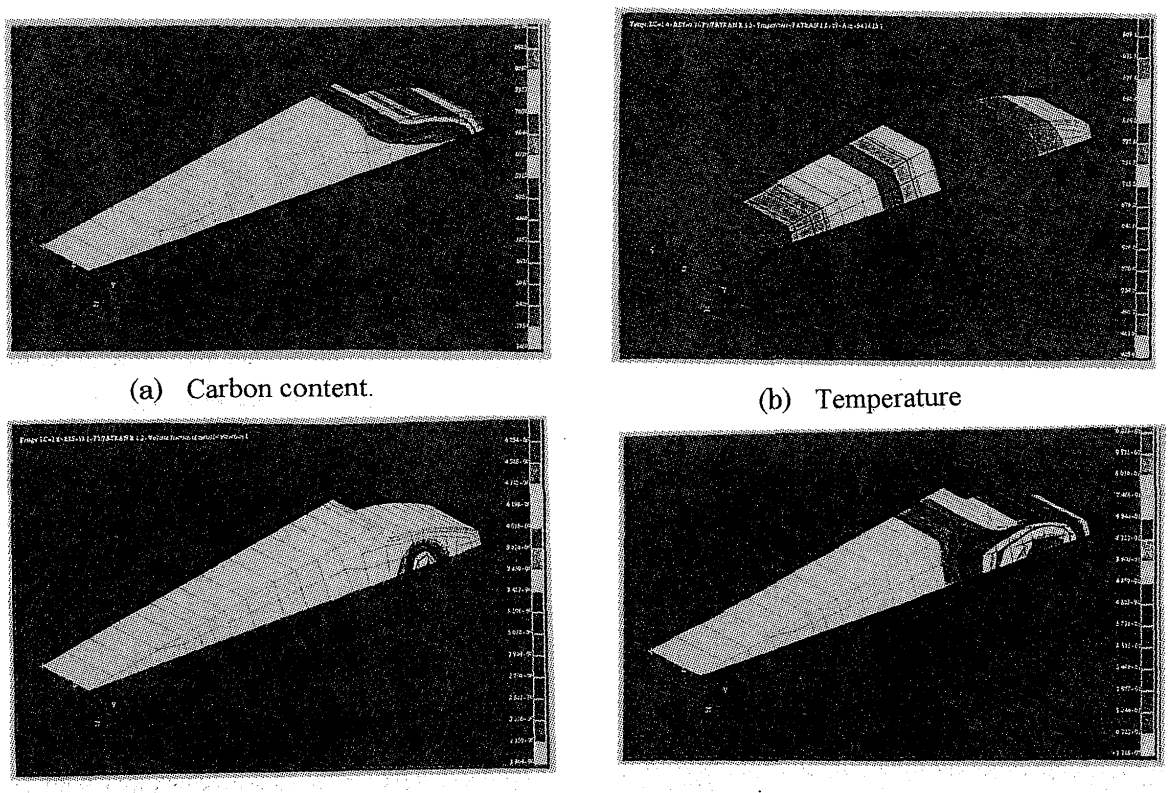

(a) Carbon content.

(b) Temperature

(c) Progressive martensite.

Fig. 9 Calculated results

external environments is C=1.0% for 0-120 min. and 0.8% for 120-210 min. Furthermore in the diffusion stage, no carbon flux from external environments is assumed on all boundaries. The boundary conditions for heat conduction analysis are such that convection from oil boundaries occur according to the convection coefficient (2093.4 W/(m^{2}K))

The simulated results are shown in **Fig. 9**. Figure 9(a) shows the distibution of carbon content after carburizing process, and Fig. 9(b) illustrates the distribution of temperature during quenching (t=30 s). Figures 9(c) and (d) depict the distribution of volume fractions of martensite during quenching. Residual stress distributions (axial and circumstantial com-

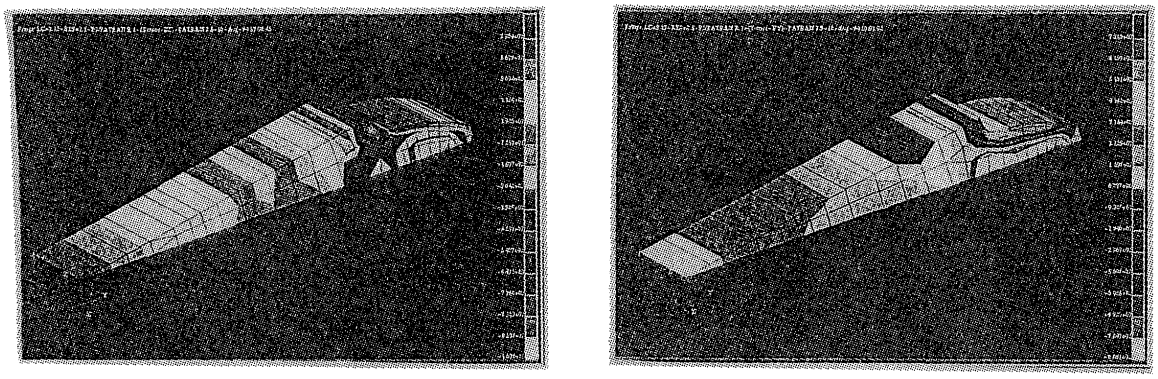

(a) Radial stress (b) Axial stress

Fig. 10 Residual stresses.

ponents) are represented in **Fig. 10** (a) and(b), respectively. The fact that the tensile residual stress in circumstantial direction is observed beneath the tip corresponds to the practical experience of case hardened gear, which results to the decrease in bending fatigue strength.

Induction hardening of a ring

Induction hardening process is also possible to be simulated by the system HEARTS. The model is a ring with the dimension of 100 and 75 mm in outer and inner diameter and 24 mm in height. The upper half of the ring is modeled as the axisymmetric problem. Induction heating is made on the outer surface with expected hardening depth of 2 mm during 4.0 sec heating period, followed by cooling. Materials employed are carbon steel(45C), Cr-Mo steel (SCM440) and Ni-Cr steel(SNC815)with hardenability, and stainless steel (SUS304) without hardenability for comparison.

The heat generation during induction heating is assumed to occur in the area of 2.0 mm in depth from the outer surface. The heat generation rate was determined by trial and error so that the maximum temperature at the surface reaches the measured value. All surfaces are regarde as adiabatic boundary during heating process, while in cooling process the outer surface is defined asthe convection boundary with uniform and constant convection coefficient 20,000W/(m^{2}K).

To know the effect of hardenability, or phase transformation on some parameters, calculation of temperature, structures, distortion and stress are compared for typical two steels of plain carbon steel and SUS304 in **Fig. 11**.

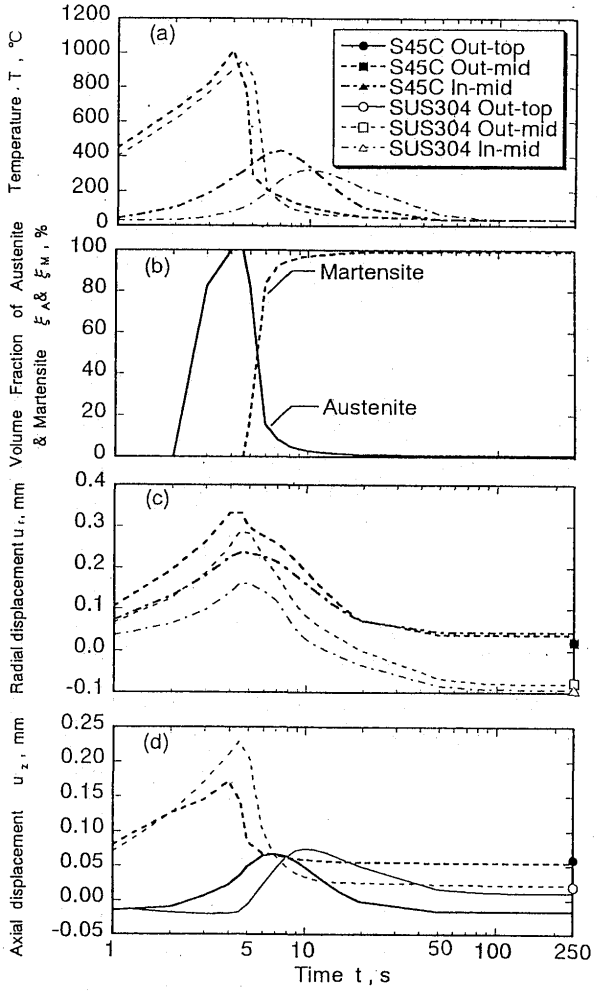

Fig. 11 Variation of temperature (a), volume fraction of austenite and martensite (b) and radial (c) and axial (d) displacement

Such effect is characterized for distortion for 4 steels as seen in **Fig. 12** with triangles indicating measured data: Volumetric dilatation due to martensitic transformation is seen to give

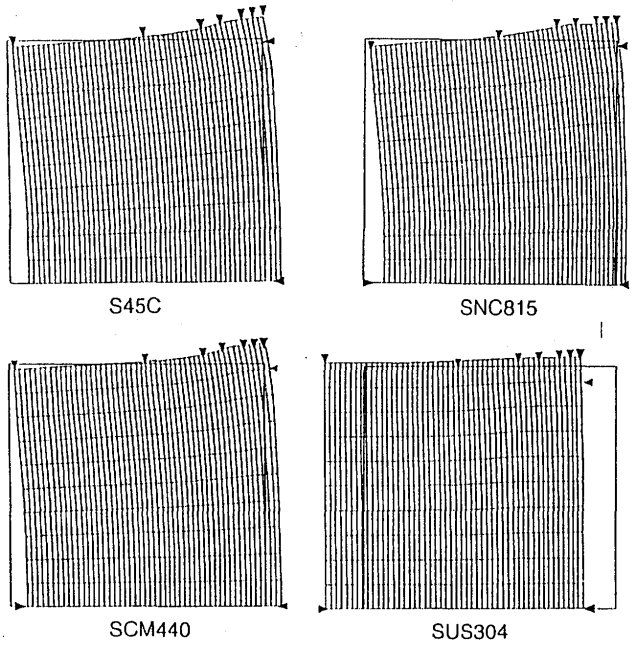

Fig. 12 Mode of distortion depending on material.

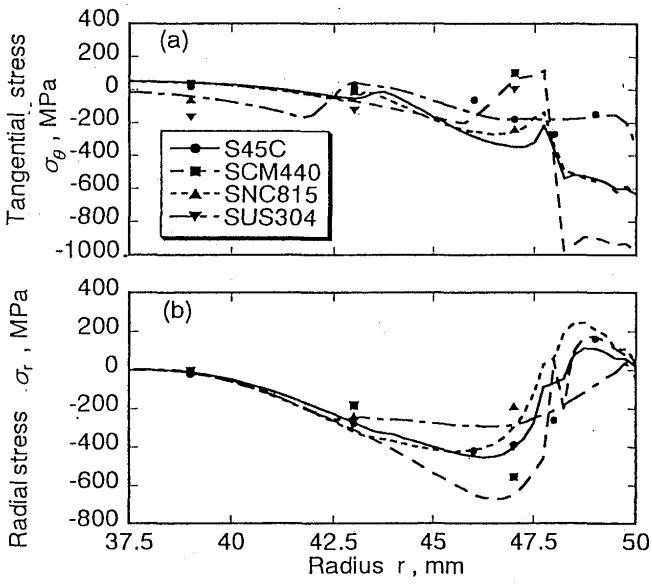

Fig. 13 Residual stress distribution of axial (a) and tangential (b) componeny on the outer surface

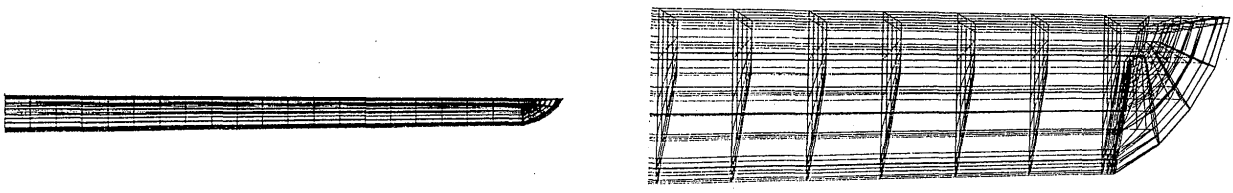

(a)Global view (b)Near the top

Fig. 14 Finite elements division of a Japanese sword

the expansion of radius (See Figs.(a), (b) and (c)), while Shriking occurs for SUS3404. **Figure13** depicts the radial residual stress distribution indicating that wavy pattern is observed in SUS 304 steel.

Quenching of a Japanese sword

The final example treats the quenching process for a Japanese sword[20,21] with the shape shown in **Fig. 14**, which is a model of a classical and famous sword *Bizen-Osafune*. Three dimensional finite element mesh division is made for half part in the width direction due to symmetry. Total number of elements is 805, and that of the nodes is 1152. The model is composed of two kinds of materials; high carbon steel, or *hagane*, in the blade part and low carbon steel, or *singane*, in the other part.

Before quenching, mixed clay with powders of charcoal aad whetstone, *yakibatsuchi*, is pasted on the surface of sword to control the heat transfer coefficient. The thickness on the back is about 1.0mm and 0.1mm on the blade. Relattive heat transfer coefficient on the surface of the steel depends on the thickness of clay as shown in **Fig.15**[13]. The sword is uniformly heated up to 850℃ and is quenched into the water of 40℃.

Figure 16 illustrates the temperature distribution of the sword with successive time from the beginning of the quenching, and the mode of deformation is also depicted in the figure. The part of blade with thin thickness shrinks by thermal contraction due to severe cooling, which leads to the bending to the downward termed as *gyaku-sori* or reverse bending. However, when martensitic trans-

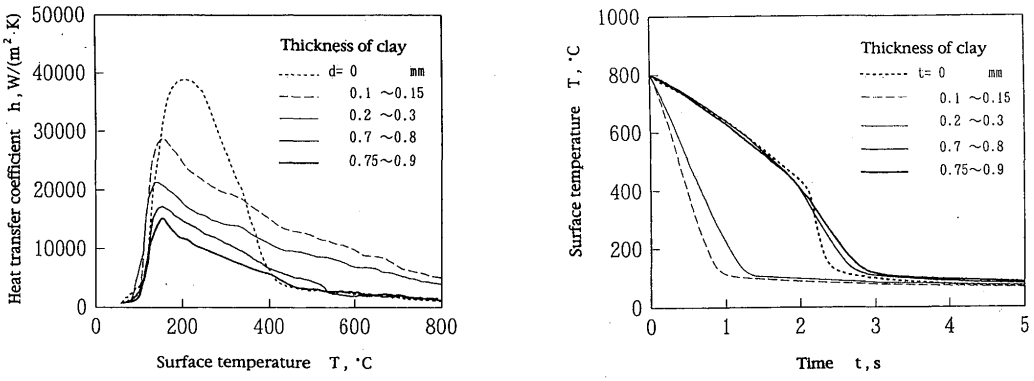

Fig. 15 Cooling curves and identified heat transfer coefficient depending on the thickness of cray.

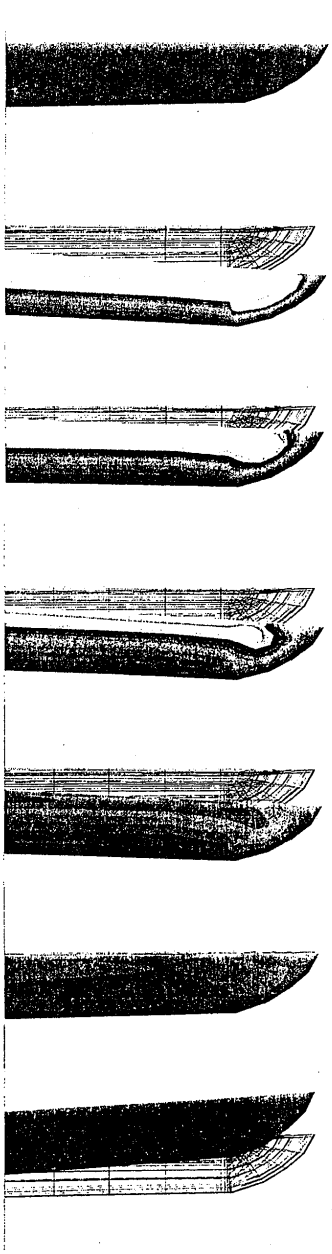

Fig. 16 Change in temperature distribution associated with deformation

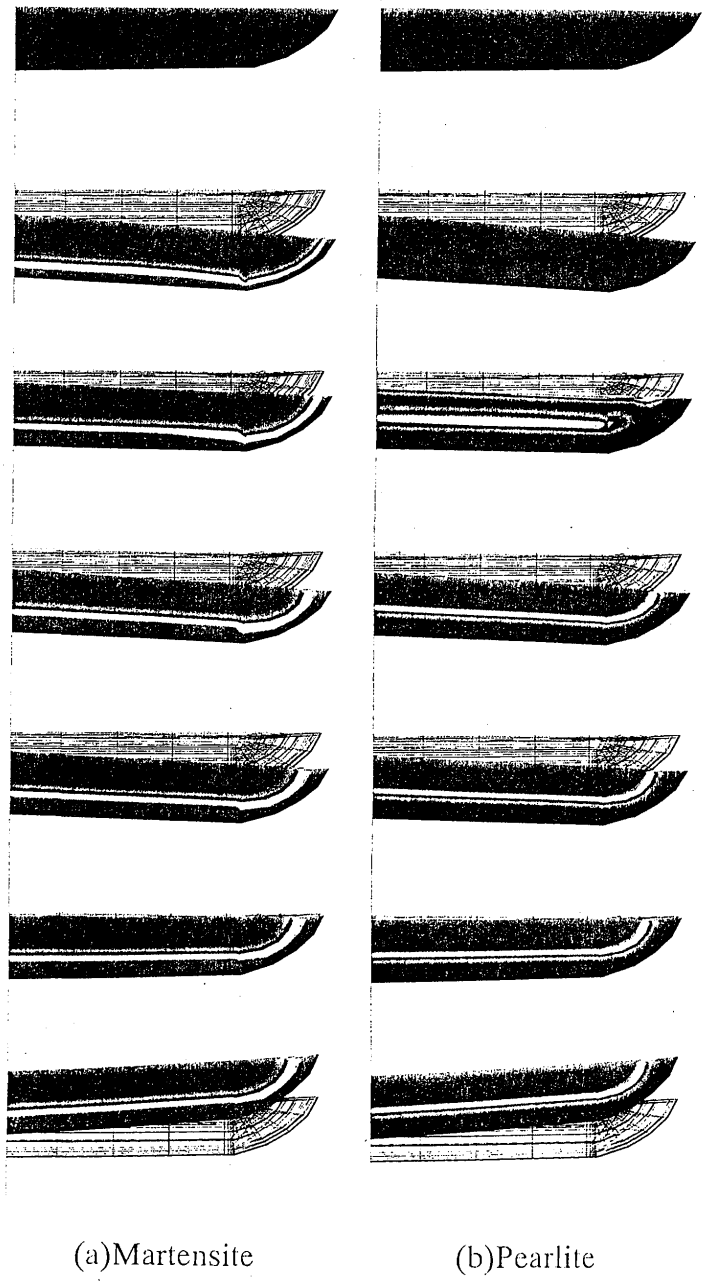

Fig. 17 Variation of martensite and pearlite.

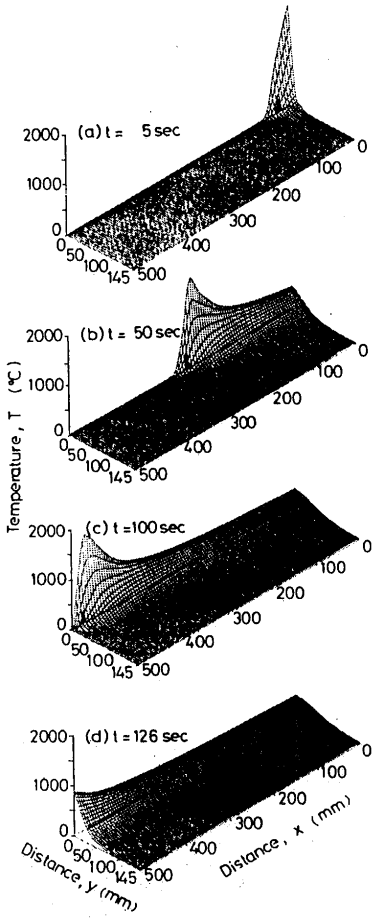

Fig. 18 Variation of temperature distribution

formation starts to occur in that part, normal bending or *sori* again appears, because of the pearlitic transformation in the part of back. In the successive stage, back side shrinks gradually because of thermal contraction, and finally, the normal bending can be obtained owing to the difference of the coefficient of dilatation by martensitic and pearlitic trans-formation as shown in **Fig. 17**.

6.2 Welding

Butt welding of plates

Two rectangular plates of 500mm × 145mm × 8mm in carbon steel for welded structures (SM41) were butt-welded under conditions of 170A and 28V with a steady electrode-travel speed of 4.7mm/s along the longitudinal direction[22]. The calculated profiles of tem-perature are successively shown in the birds-eye view of **Fig. 18**, and the variation of the temperature at several points is given in **Fig. 19** with data

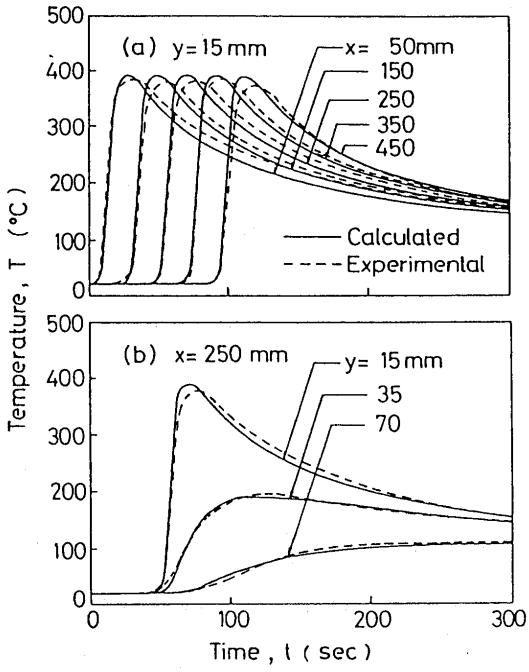

Fig. 19 Comparison of calculated and measured temperature

measured by thermocouples. Both the calculated and experimental results show the temperature changes according to the travel of the electrode.

Since the thickness of the plate was small enough compared with other dimensions, plane stress conditions are assumed throughout the stress analysis. The calculated distribution of stress is partly shown in **Fig.20**. It is shown that residual stress $\sigma_x(t=\infty)$ at the periphery of the welding line is as high as the flow stress except at both edges, and the peaks in σ_y appear at about 100mm inside the edge. The residual stresses at the mid-section of the plate are plotted in **Fig.21** with the experimental data measured on the upper and lower sides of the plate by the X-ray diffraction technique.

Bead-on plate

The second example related to welding is a bead-on-plate simulation of traveling electrode[23], and the precise feature in the hatched cross sectional region in **Fig.22** is carefully discussed. Electrode is assumed to travel along x-axis at a velocity of 5mm/s. Quantity of heat supply is 4000 W, bead width is 6mm and then the time required for heat supplying is 1.2sec.

Figure 22(b) indicates the finite element mesh division with elements 279 and the nodes

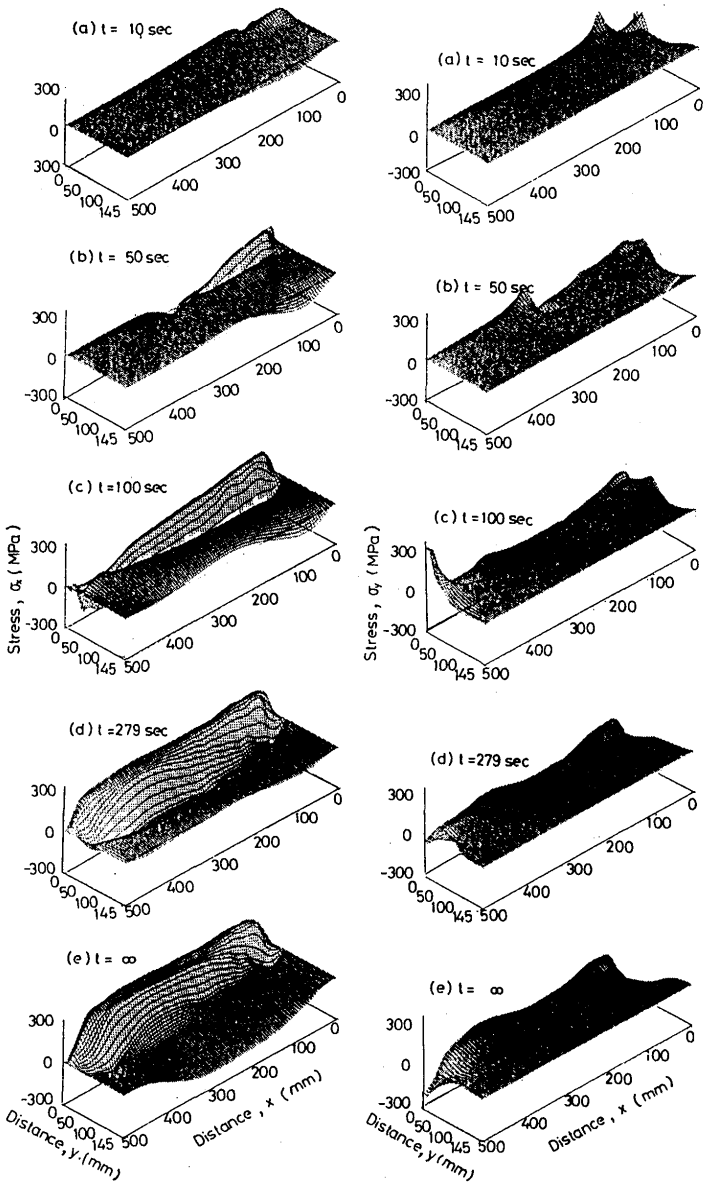

Fig. 20 Variation of stresses.

169. Restraint for mechanical analysis is shown in Fig.(c) in order to express the deformation depending on thermal, transformation and visco-plastic strain effectively.

Calculated results are shown in Fig.23. Left side is z-axis and the heat is supplied from upper side. In the beginning of welding operation, the supplied heat is mehing the part of upper side, and the deformation caused by thermal and transformation strain is observed as shown in Fig. 23(a). Molten pool is growing and the deformation becomes increasingly conspicuous with the progress of the operation. The difference of flow between liquid and solid phases is apparent at t =0.6 sec as seen in Fig(b)

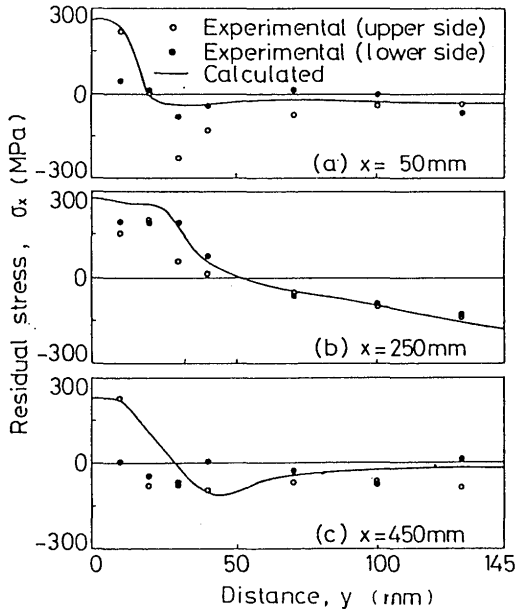

Fig. 21 Comparison of calculated and measured residual stresses.

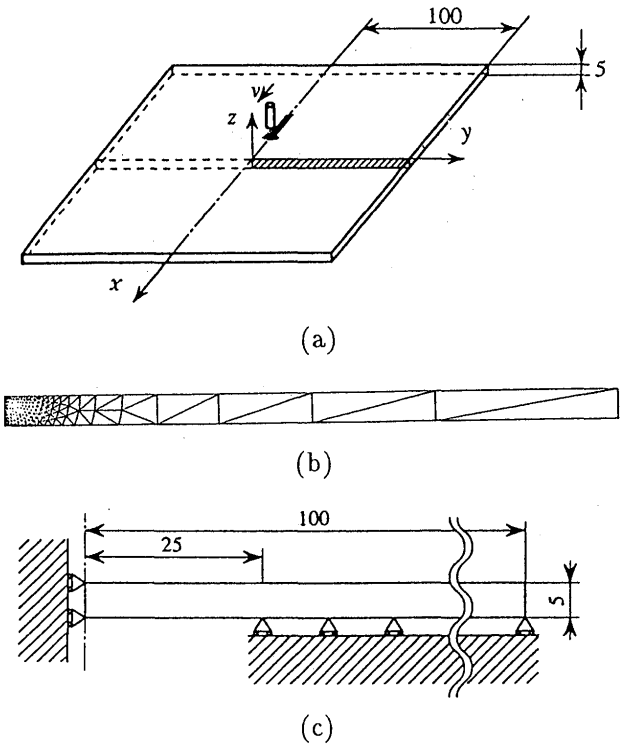

Fig. 22 Model of bead-on-plate.

6.3 Casting

Continuous casting

Many investigations to simulate the continuous casting process have employed a simplified model, in which motion of a part of the slab moving through the mold and spray zone is

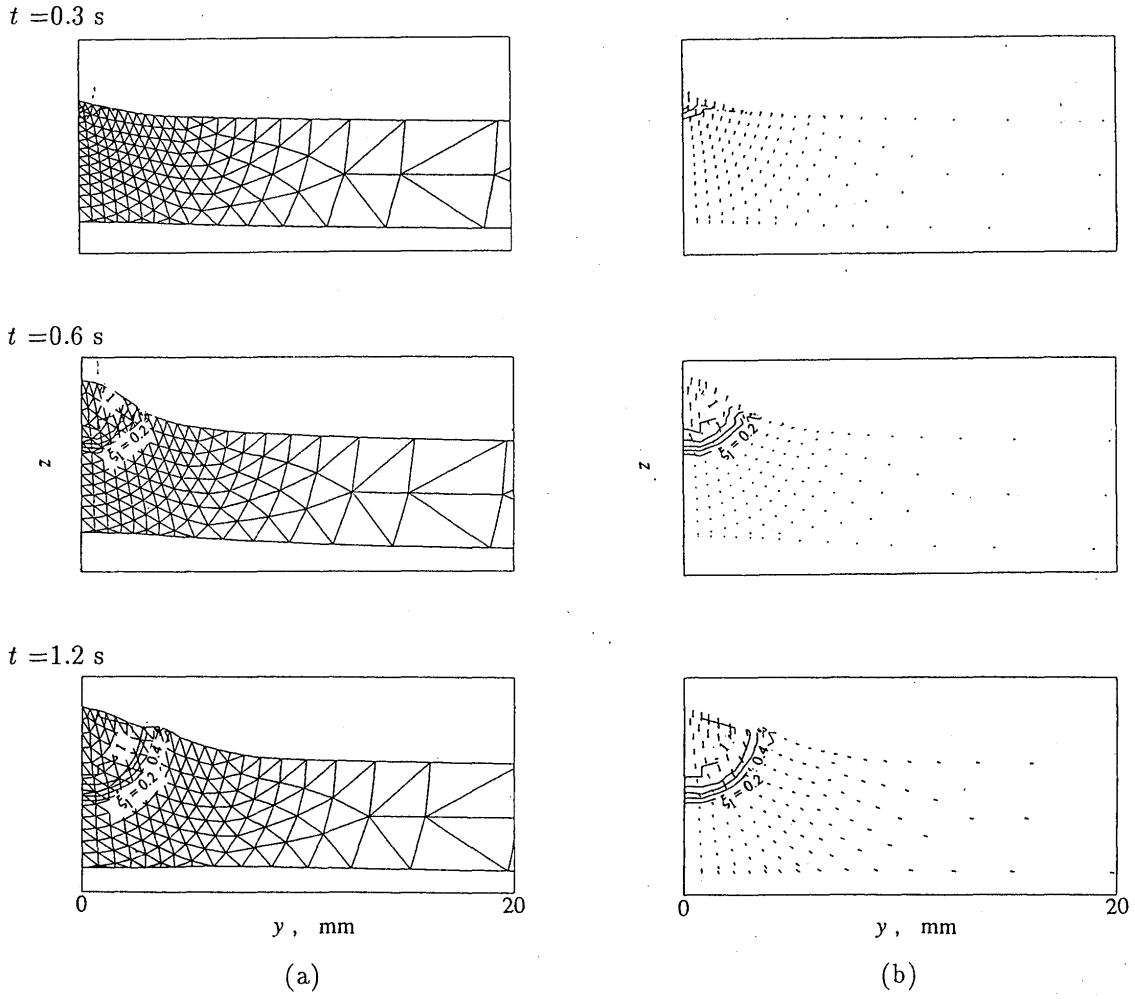

Fig. 23 Deformation (a) and material flow (b) during welding.

expressed in a material coordinate system subjected to unsteady boundary con-ditions (See **Fig. 24**(a)). In this method, the heat flow in the casting direction, and especially the effect of the external force or constraint on displacement from the rollers and gravitational force cannot be allowed for.

Here, we shall formulate the equations governing the temperature and stress fields in a spatial coordinate system as shown in Fig. 24(b)[24]. Suppose that the motion of material point X_i at time t is expressed in a spatial coordinate x_i as

$$x_i = x_i(X_j, t) \tag{49}$$

Then, the material derivative of a scalar, vector, or tensor variable ψ is given by

$$\dot{\psi} \equiv \frac{D\psi}{Dt} = \frac{\partial \psi(X_i,t)}{\partial t} = \frac{\partial \psi(x_i,t)}{\partial t} + \frac{\partial \psi(x_i,t)}{\partial x_k} v_k \tag{50}$$

with velocity v_i and heat conduction equation (40) is reduced to

$$\rho c \frac{\partial T}{\partial t} + \rho c v_i \frac{\partial T}{\partial x_i} - \frac{\partial}{\partial x_i}\left(k \frac{\partial T}{\partial x_i}\right) = \rho l_A \frac{\partial \xi_A}{\partial t} + \rho l_A v_i \frac{\partial \xi_A}{\partial x_i} \tag{51}$$

neglecting the heat generation due to mechanical work. In the steady state, $(\partial()/\partial t = 0)$, Eq.(51) becomes

$$\rho c v_i \frac{\partial T}{\partial x_i} - \frac{\partial}{\partial x_i}\left(k \frac{\partial T}{\partial x_i}\right) = \rho l_A v_i \frac{\partial \xi_A}{\partial x_i} \tag{52}$$

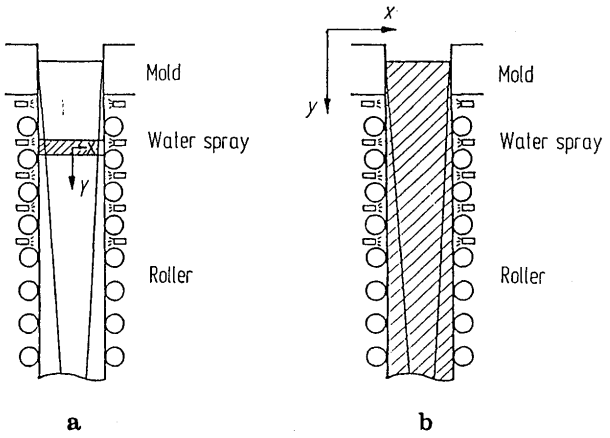

Fig. 24 Models of continuous casting

Since Eq.(52) includes no derivative of temperature, it can be directly solved to get the temperature distribution under the fixed and natural boundary conditions

$$\begin{aligned} T &= \bar{T} && on \quad S_T \\ kn_i \frac{\partial T}{\partial x_i} &= h(T - T_W) && on \quad S_h \end{aligned} \tag{53}$$

with heat transfer coefficient h and ambient temperature T_w. We also take the material derivative in the governing equations necessary for stress analysis:

$$\dot{\varepsilon}^e_{ij} = \frac{1+\nu}{E}\dot{\sigma}_{ij} - \frac{\nu}{E}\delta_{ij}\sigma_{kk} + \left[\frac{\partial}{\partial T}\left(\frac{1+\nu}{E}\right)\sigma_{ij} - \frac{\partial}{\partial T}\left(\frac{\nu}{E}\right)\delta_{ij}\sigma_{kk} + \alpha\delta_{ij}\right]\dot{T} + \sum_{I=1}^{N}\delta_{ij}\beta_I\dot{\xi}_I \tag{54}$$

$$\dot{\varepsilon}^i_{ij} = \frac{1}{3\mu}\psi(F)\frac{\partial F}{\partial \sigma_{ij}} \tag{55}$$

$$\frac{\partial \dot{\sigma}_{ij}}{\partial x_i} + \rho \dot{b}_i = 0 \tag{56}$$

$$\dot{\varepsilon}_{ij} = \frac{1}{2}\left[\frac{\partial \dot{u}_{ij}}{\partial x_i} + \left(\frac{\partial \dot{u}_{ij}}{\partial x_i}\right)^T\right] \tag{57}$$

$$\begin{aligned} \dot{\sigma}_{ij} n_i &= \dot{\bar{t}}_{ij} && on \quad S_F \\ \dot{u}_{ij} &= \dot{\bar{u}}_{ij} && on \quad S_u \end{aligned} \tag{58}$$

and let the time derivative $\partial()/\partial t = 0$, so that we have a set of equations involving stress σ_{ij} and

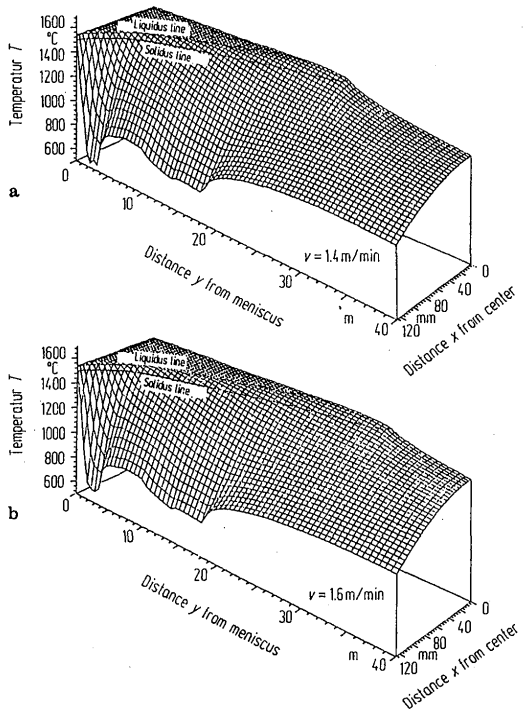

Fig. 25 Bird–eye view of temperature.

strain $\dot{\varepsilon}_{ij}$ A simple method is, however, employed to solve the equations directly to determine strain rate $\dot{\varepsilon}_{ij}$ and stress rate $\dot{\sigma}_{ij}$ by the steady boundary conditions

$$\begin{aligned} \dot{\sigma}_{ij} n_i &= \frac{\partial \bar{t}_{ij}}{\partial t} + v_i \frac{\partial \bar{t}_{ij}}{\partial x_i} = \dot{u}_{ij}\frac{\partial \bar{t}(x_i)}{\partial x_i} \\ \dot{u}_{ij} &= \dot{u}_{ij}(x_i) \end{aligned} \tag{59}$$

Then, strain $\dot{\varepsilon}_{ij}$ and stress σ_{ij} can be evaluated by integrating $\dot{\varepsilon}_{ij}$ and σ_{ij} along the path line. A slab with dimensions of 40000mm x 1250mm x 250mm in a vertical type of continuous casting process with casting speed v=1.6m/min was analyzed by the finite element method. Since the slab was wide enough compared with the thickness, a central cross section was treated as shown in Fig.24(b).

Figure 25 represents the calculated temperature distribution with liquidus and solidus lines in birds-eye views under the three casting speeds of v =1.4, 1.6 and1.8 m/min, and **Fig. 26** gives the temperature distribution and shell thickness (solid lines) in a sectional plane. In the early stage near the mold, the temperature on the surface decreases rapidly owing to the extreme cooling conditions, but when the cooling

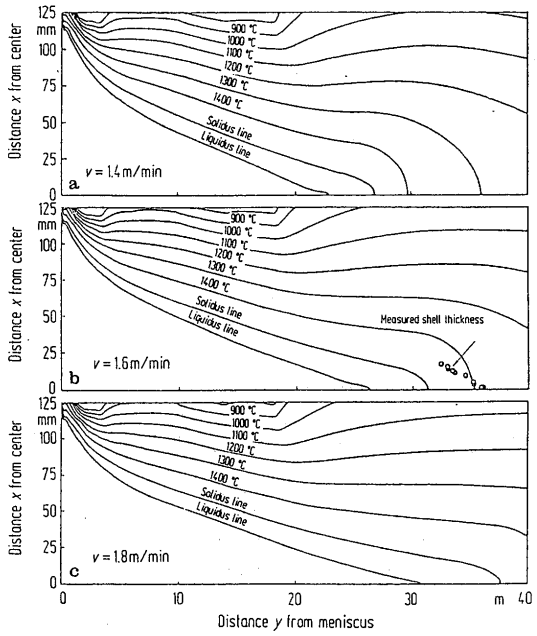

Fig. 26 Temperature distribution of cross–section with experimental data of shell thickness.

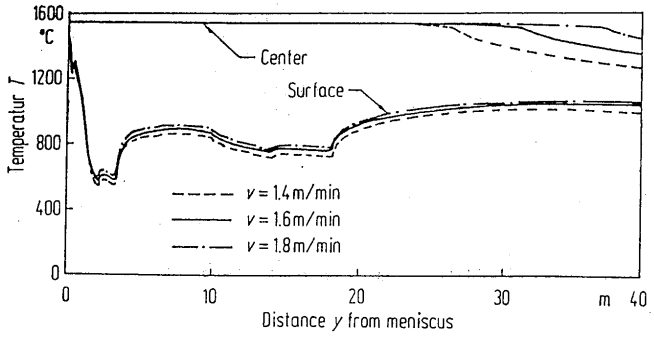

Fig. 27 Temperature variation depending on casting velocity

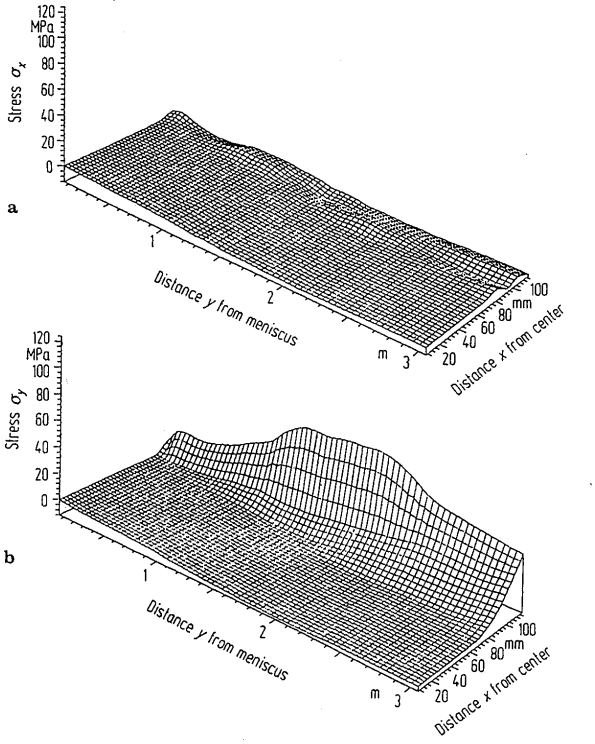

Fig. 28 Stress distribution in solidified shell.

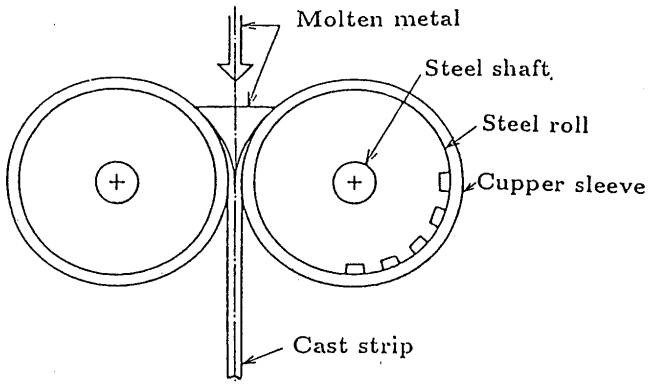

Fig. 29 Thin slab casting system.

rate lessens later, the slab is again reheated owing to the latent heat produced inside the molten metal. The change in casting speed affects the temperature and shell thickness distribution represented by solid lines in Fig.26, which shows good agreement with experimentally measured data. In spite of the increasing temperature at the center of the slab with increasing speed, the temperature on the surface is hardly affected by the speed, as shown in **Fig.27**. The calculated distributions of normal stresses in the longitudinal and lateral directions are shown in **Fig.28**. The stress level is known to be rather low in the central part of the slab, which is in a liquid state, while longitudinal stress σ_y is markedly raised near the surface owing to solidification.

Thin slab casting

The technique of thin slab casting (See **Fig.29** illustrating the twin roll casting system[25], one of the techniques) is an exciting project to save energy for rolling in steel making process. The experiment, however, cost a lot which is the reason why the simulation gives the beneficial tool.

The mesh division of the main part of the system including the roll is shown in **Fig.30**. Calculated temperature distribution in the steady operation is shown in **Fig.31**, and the distribution of fraction of solidified phase and

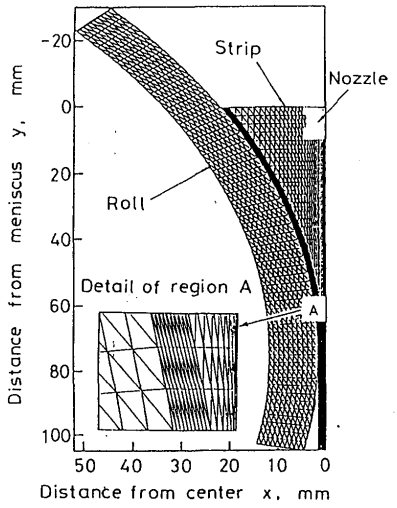

Fig. 30 Mesh pattern for slab and roll

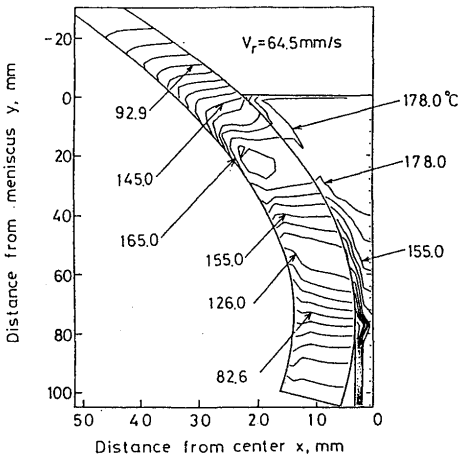

Fig. 31 Temperature distribution

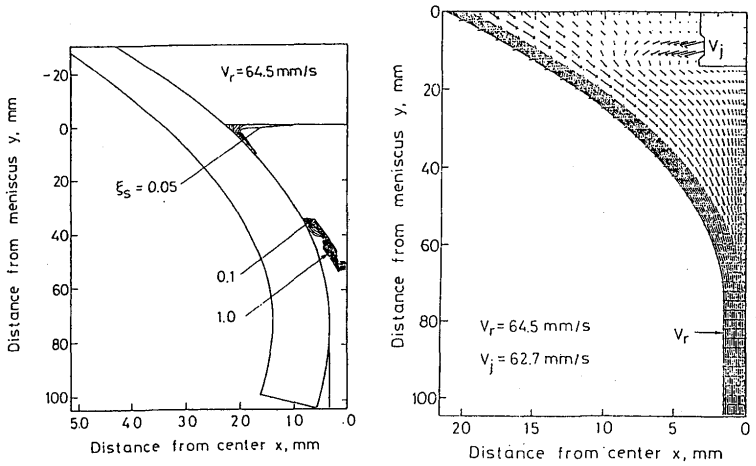

Fig. 32 Solidifying fraction (a) and velocity field (b).

the velocity field are respectively represented in **Fig.32**(a) and (b). Stress distribution in the flow direction at some cross section of the slab is also depicted in **Fig.33**.

Centrifugal casting

Main feature of this type of casting[25-26] is that the region to be analyzed as well as the location of interface of solid and liquid is not a steady, but moves with time, which is called growing and moving boundary problem. In this case of axisymmetric problem of manufacturing a tube, new finite elements are successively added on growing boundary.

Comparison of the simulated and measured temperature variation on the inner surface of a tube is represented in **Fig.34**, and the progressive mode of solidification is depicted in **Fig.35**, and the change in stress distribution is shown in **Fig.36**.

Manufacturing of functionally gradient tube

When the material to be poured in the process of centrifugal casting is altered in progressive time, say, by artificially changing the fraction of reinforcements, or by the movement of reinforce particles due to centri-fugal force, it is possible to make a tube with functionally gradient property[27-28].

Figure 37 illustrates an example of volume fraction of progressive solid phase, and the comparison of calculated and experimental distribution of density of particles is shown in **Fig.38** as the function of rotating velocity.

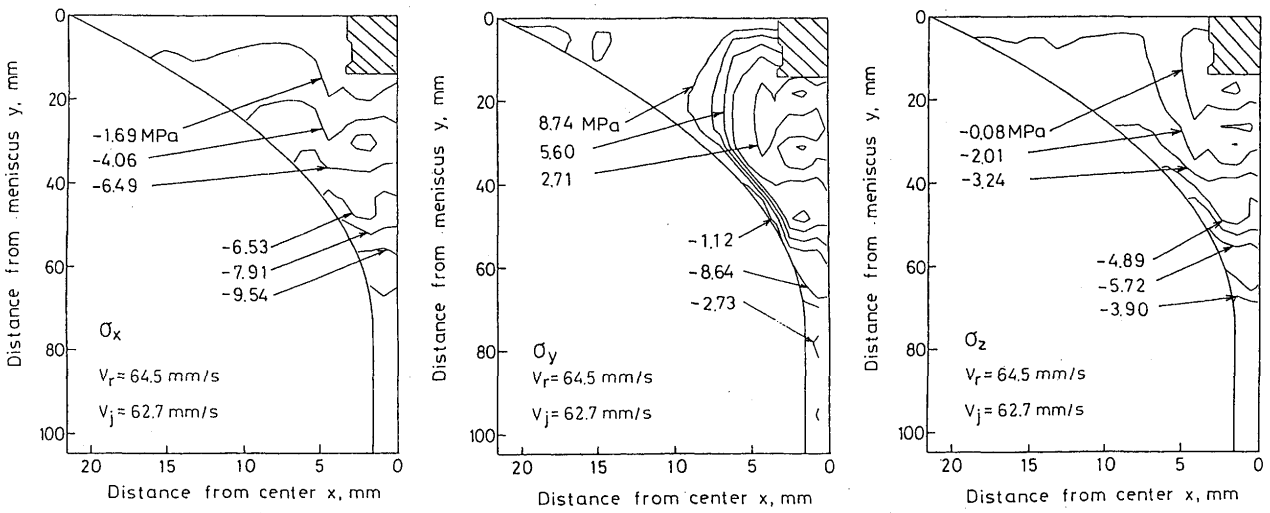

Fig. 33 Stress distribution

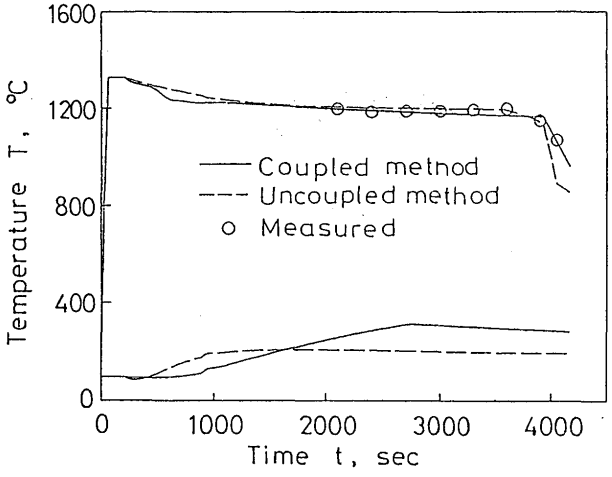

Fig. 34 Change of temperature at inner surface.

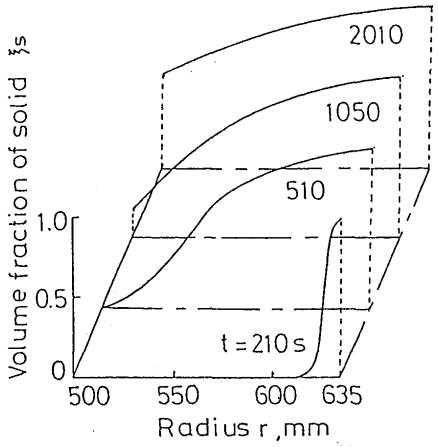

Fig. 35 Progress of solidifying domain

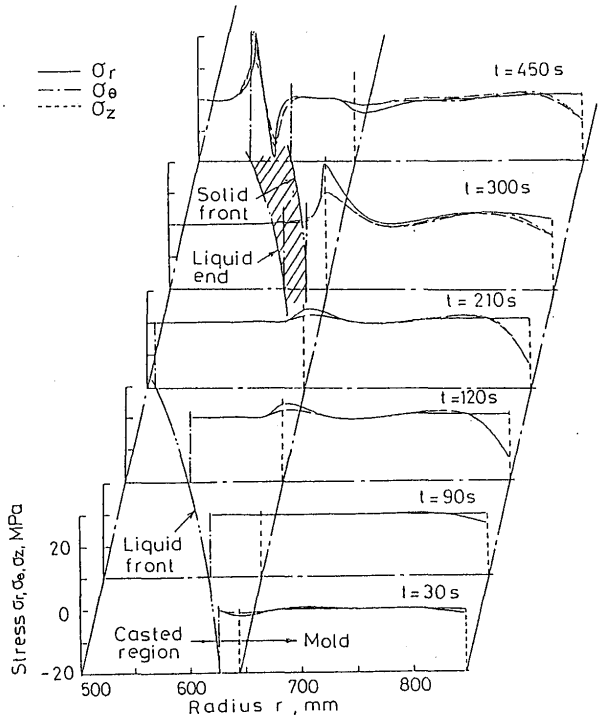

Fig. 36 Change in stress pattern.

7. Concluding Remarks

Fundamental equations governing the temperature, stress and metallic structural distribution in steel undergoing phase transformation have been developed when the coupling effect between them is taken into account, and the procedure for solving the equations by the finite element method has been presented. Applications of the theory were carried out to simulate the engineering processes of carbu-rized quenching, butt-welding and continuous casting. The calculated results of the tem-perature, stress and structural change were compared with the experimentally measured data to confirm the

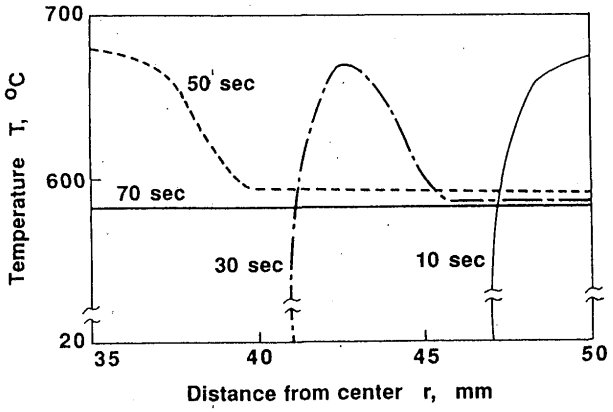

Fig. 37 Mode of progressing domain

validity of the simulation.

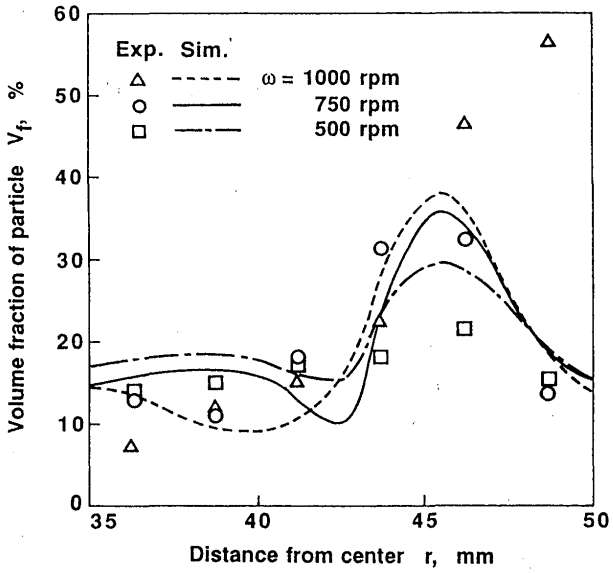

Fig. 38 Distribution of fraction of reinforcement.

References

1) T. Inoue, S. Nagaki, T. Kishino and M. Monkawa, Ing.-Archives., 50, 5 (1981) 315-327
2) T. Inoue, Thermal Stresses (Ed. Richard B.Hetnarski), 1988, North-Holland, 192-278
3) T.Inoue,.Computational Plasticity---Current Japanese Materials Research Vol. 7 (1990) (Ed. T. Inoue, H. Kitagawa and S. Shima), 1990, Elsevier Applied Science, 73-96
4) T. Inoue and B. Raniecki, J. Mech. Phys.of Solids, 26, 3 (1978) 187-212
5) T. Inoue Berg- und Huttenmaannische Monatshefte, 132,.3(1987).63-7 1
6) R. M. Bowen: Continuum Physics, Vol. 3, Academic Press, New York (1976)
7) L.E.Malvern, Introduction to the Mechanics of Continuous Medium, Prentice-Hall, 1969
8) P. Perzyna: A&. AppI. Mech., 9, (1979)3 15.
9) Z. G. Wang and T. Inoue, Material Science and Technology, 1 (1985-10) 899-903
10)A.W.Johnson and R. F. Mehl: T 416.
11) C. L. Magee: Phase Transformations, Chapman Hall, London, (1979) 115.
12) S. Bhattacharyya and G. L. Kel, Trans. ASM,47(1955) 351-279
13) H. Onodera, H. Gotoh andI. Tamura, Proc. lst JIMInt. Symp. New Aspects of Martesitic Transformation,(1976) 327-332
14) T. Inoue, K. Arimoto and D.Y. Ju, Proc. Ist Int.Conf. Quenching and Control of Distorsion, Chicago, (1992) 205-212
15) T.Inoue, K. Arimoto and D-Y.Ju., Proc. 8th Int. Congr. on Heat Treatment of Materials, Kyoto, (1992)569-572
17) T. Inoue and K. Arimoto, J. Materials Reng. and Performance, ASM(to appear)
18) K,J, Bathe, Finite Element Procedure in Engineering Analysis, Prentice-Hall, 1982
19) T. Inoue, H. Inoue, T. Uehara, F. Ikuta, K. Arimoto and T. Igari, Proc. 2nd lnt. Conf. Quenchtng and Control of Distorsion, Cleveland (1996)(to appear)
20) T. Inoue, T. Ohmori, T. Hanabusa and H. Fujiwara Proc. 4th Int. Conf. Residual St-resses, Baltimore,(19943) 970-976
21) T. Inoue ,T. Uehara and Y.Nakano, Proc.5th Int. Sym.Plasticity and its Current Applications, Sakai-Osaka,(1995)697-700
22) Z.-G. Wang and T. Inoue ,Material Science and Technology, 1. I (1985) 899-903
23) A. Sakuma and T.Inoue, Proc. 5th Int.Symp. on Plasticity and its Current Applications. Sakai- Osaka.(1995)721-724
24) T. Inoue and Z. G. Wang, Ingenieur-Archiv. 58-4 (1988) 265-275
25) T. Inoue and D.Y. Ju. Advances in Continuum Mechanics (Ed. O. Bruller,V. Mannl and J. Najar),Spinger-Verlag, 1991, 389-406
26) D.Y. Du and T. Inoue, Proc. Int. Conf. on Computer- assisted Materials Design and Process Simulation, Tokyo, 1993,84-89
27) M. Mizuno, T. Matsuoka and T. Inoue, Proc. Int. Conf. on Computer-assisted Materials Design and Process Simulation, Tokyo, 1993. 30-35
28) M. Mizuno, T.Matsuoka K. Abe and T. Inoue, Proc. Symp. on Novel Technique in Synthesis and Processing of Advanced Materials, ASM, 1995, 415-418